IEEE Access
Multidisciplinary ⋮ Rapid Review ⋮ Open Access Journal

Received 28 October 2024, accepted 31 December 2024, date of publication 9 January 2025, date of current version 15 January 2025.

Digital Object Identifier 10.1109/ACCESS.2025.3527873

RESEARCH ARTICLE

Design and Analysis of a Parallel Elastic Shoulder Joint for Humanoid Robotics Application

SHARAFATDIN YESSIRKEPOV, TIMUR UMURZAKOV, AND MICHELE FOLGHERAITER, (Member, IEEE)
Department of Robotics, School of Engineering and Digital Sciences, Nazarbayev University, Astana 01000, Kazakhstan

Corresponding author: Sharafatdin Yessirkepov (sharafatdin.yessirkepov@nu.edu.kz)

This work was supported by Nazarbayev University under the Faculty Development Competitive Research Grants Program through the Project "Designing an Energy-Efficient Full-Sized Humanoid Robot With Fast Adaptive Model-Based Neuromorphic Control Architecture" under Award 201223FD8812.

ABSTRACT This paper presents an innovative hybrid cable-driven shoulder joint for humanoid robotics application. A blend of a flexible central limb and three rigid lateral limbs, form a 2-degree-of-freedom (2 DOF) mechanism that connects the mobile platform to the fixed base. This design leverages both good mechanical stability and the integration of an elastic element, which mitigates vibrations up to 40% and allows the storage and release of elastic potential energy up to $1.9\,J$. Initially, three alternative and incremental shoulder joint designs are presented and evaluated across two distinct experiments: 1) Energy storage analysis of the parallel mechanism during single cable motion and 2) Dynamic response and vibration damping. Following these experiments, a detailed analysis is performed on the stiffness properties of the proposed prototype, as it outperforms the other two designs. The dimension of the central elastic limb, made out of Thermo-Plastic Polyurethane (TPU), is optimized using Finite Element Analysis (FEA). The kinematic behavior of the proposed mechanism is approximated as a combination of linkages equipped with two universal joints, and its motion evaluated through numerical simulations and real experiments.

INDEX TERMS Parallel robots, soft robotics, energy storage, shoulder joint, cable-driven mechanism.

I. INTRODUCTION

Designing and optimizing parallel kinematic architectures is a prominent area of research in robotics. Opting for a closed-loop kinematic structure over an open-loop kinematic one is preferable for some of the humanoid robot's joints, as it helps minimize the weight and inertia of the upper links of the arms [1] and legs, decrease energy consumption, and enhance precision and workload capabilities of the end-effector.

Work on parallel manipulators (PMs) began in the 1960s, leading to the development of several kinematic architectures consisting of rigid limb attachments between the base and the moving platform. Significant examples from the period between the 1960s and 1980s include the Gough-Stewart Platform [2], the Delta Robot [3], and the Tripod Manipulator [4]. Since the 1990s, three main categories of closed-loop kinematic chains have gained popularity: Cable-Driven Parallel Manipulators (CDPM) [5], Compliant Parallel Manipulators [6], and Redundant Parallel Manipulators [7].

The use of a cable-driven mechanism is aimed at reducing the weight-to-power ratio of the parallel manipulator. Additionally, compared to conventional closed-loop kinematic systems, cable-driven parallel mechanisms offer more cost-effective and energy-efficient performances with an extended workspace [8].

Flexible and compliant parallel manipulators are used in various applications that require tasks like precise movement in medical surgery works [9], vibration damping in manufacturing process [10], and energy storage. Their ability to handle such tasks is largely due to their design, which incorporates elastic components for flexibility and adaptability.

Recent works have been dedicated to various research problems related to parallel manipulators, including stiffness

The associate editor coordinating the review of this manuscript and approving it for publication was Guilin Yang.

analysis [11], [12], [13], [14], dynamic computations and vibration control [15], [16], [17], [18], [19], [20], [21], workspace optimization [22], [23], [24], enhancement of kinematic accuracy and workload capacity [25], [26], [27], integration of elastic links [13], [28], compression analysis [29], [30] and trajectory planning [31].

Advanced closed-loop kinematic chains, such as those discussed in [12], [32], [33], [34], and [35] focused on rigid leg-based structures connecting the fixed and moving platforms. In [12], the stiffness analysis of a 3DOF 2SPR+RPS parallel manipulator involved testing the elastic deformations of the platform at various joint positions and external loads. A prototype of high stiffness and low inertia shoulder joint mechanism was analyzed in [33], where a comparison employing two legs, three legs, and four legs was performed, ultimately affirming the superiority of the three-limb structure in achieving high motion within a 3D space. In other words, the platform was connected to the base via three limbs, offering optimal freedom of movement without the generation of any singularity within the workspace. In another study [34], the analysis focuses on a shoulder design featuring carbon fiber links, allowing precise control over its compliance characteristics. The impulse responses of two types of carbon fiber links were compared. The results indicated that the second wide link combined with a damper, exhibited higher precision and stiffness compared to the first narrow link without the damper.

In [32], a parallel manipulator was developed for rehabilitation purpose, where both position and force controlling strategies of the system were investigated.

The dynamic behavior and response of parallel mechanisms were analyzed in other studies [15], [16], [17], [18], [19], [20], [21]. In [15] it was verified that the presence of the elastic element minimized the vibration in the system. The elastic cable indicated a higher time-delay effect during the oscillation process of the manipulator compared to a non-elastic cable. In [18], the vibration of a planar robotic finger was minimized by applying a weight at the end-effector and attaching a spring pair at each joint. In addition, the springs helped increasing the stiffness and motion range of the end-effector. In [19], the Euler-Lagrange method was employed to model the dynamic and kinematic behaviors of a cable-driven continuum robot (CDCR), while the sagging effect of the cables was investigated in [20]. The researchers developed a wave-based control technique that utilized both the position of the end-effector and the vibration control capabilities of the cable.

Some research groups dedicated effort to optimize the motion and workspace of the end-effector [22], [23], [24]. In [22], a parallel manipulator was integrated with a serial manipulator and it was verified that the new hybrid mechanism achieved an expanded workspace. As a practical application, [23] demonstrated that it is possible to use parallel manipulators in agriculture to achieve precise spraying to the morphological centers of weeds and thus minimize the excessive use of herbicides on plants. In [24], the dimensionally homogeneous constrained-embedded Jacobian and T-mechanism were introduced to optimize the complex and nonparasitic motion within the workspace for a 3 PRS parallel manipulator.

In the field of humanoid robotics, certain cable-driven parallel manipulators (CDPMs) have been extensively utilized. The central link of a closed-loop kinematic chain can be designed in the form of a helical spring or cylindrical elastic shape, which has a bending ability and can be integrated with additional tendons attached between the base and moving platform [13], [28], [29], [30]. A CDPM with a spring-based central leg was designed in [28]. To overcome the spring vibration problem, a nonlinear control method was introduced. Similarly, the Cable-driven Series Parallel Manipulator (CDSPM) in [29] featured an adjustable stiffness spring integrated with a universal joint-based central rigid leg. A Finite Element Analysis (FEA) was developed to model the static forces, particularly to understand the bending and compression behaviors of the spring. In [13], a CDPM with a central rubber supporting rod and four lateral cables was tested based on the load moment applied on the platform. The researchers described the structure of the shoulder and wrist joint using screw theory. The total stiffness, combining the cable and spring stiffness, was computed in [30], and it varied based on the analysis of a rigid-flexible coupling experiment.

As elastic materials have a bending ability without significant deformation, their usage to build parallel manipulators can change the mechanism stiffness, damp vibrations, and store and release energy. The dynamic behavior of a cantilever beam connected to a spring-mass system was studied in [37]. In another experiment [38], the shape recovery of PolyLactic Acid (PLA) and TPU-based 3D materials at different temperatures were investigated. Specimens were created using Fused Deposition Modeling (FDM), comprising two layers with a thickness of 2mm each. One specimen had a PLA content as the first layer and a second layer was made of TPU material, while another specimen consisted solely of PLA material. The experimental results indicated that combining a PLA layer with TPU material exhibited a higher bending modulus and better shape recovery ability compared to the PLA-only specimen, particularly at temperatures ranging from 60 to 90 degrees. The hyper and viscoelastic behaviors of TPU and PolyDiMethylSiloxane (PDMS) dampers using Finite Element Analysis (FEA) and Dynamic Thermomechanical Analysis (DTMA) were examined in [39]. Uniaxial tension tests were performed on both materials at three different loading rates and confirmed that the PDMS damper was stiffer than the TPU damper. Similarly, the cubic samples of TPU with lattice structures were compared in terms of compression, torsion, extension, and bending behaviors in [40]. The results showed that the TPU-a sample demonstrated better energy absorption and higher stiffness than TPU-x sample. This experiment aimed to develop TPU-based InterVertebral Disc (IVD) implants

with a "Bucklicrystal" structure capable of withstanding compression and torsion from any direction.

Although numerous studies exist on various parallel manipulator architectures, and different materials have been analyzed for implementing elastic elements, there remains a need for dedicated research to investigate tendon-actuated hybrid parallel manipulators incorporating both rigid and flexible limbs.

Our methodology for developing the proposed architecture began with studying the properties of purely elastic and purely rigid joints, both utilizing the same tendon-based actuation mechanism. We then implemented a hybrid configuration that combines these two designs, allowing us to evaluate its performance and highlight the advantages of both original configurations.

This study introduces an innovative design for a shoulder joint, similar to [13], [28], [30], [33], and [41]. However, as a main difference it merges traditional inflexible limbs with a central elastic limb crafted from Thermoplastic PolyUrethane (TPU).

The primary innovation lies in the design and analysis of the hybrid parallel architecture that enhances mechanical energy storage and release, reduces vibrations, and minimizes rotational backlash in the orientation platform.

In this study, the elasticity of the TPU material is evaluated through Finite Element Analysis (FEA), while the joint's kinematic configuration, featuring a linkage and two universal joints, is detailed. Lastly, a comprehensive analysis of the kinematic and dynamic behaviors of this hybrid shoulder joint is provided, enabling 2-DOF rotational motion along the roll and pitch axes.

Compared to state-of-the-art studies on shoulder mechanisms, the main contributions of this work are as follows:

- Development of an innovative parallel manipulator architecture based on a hybrid limb configuration, consisting of a combination of rigid and elastic legs that allows reducing the energy consumption, vibrations and backlash.
- Validation of the shoulder concept is demonstrated through real experiments, showcasing the elastic central limb's ability to absorb the mechanical energy, vibrations, and minimize torsional backlash.
- Characterization of the stiffness, kinematic and dynamic behavior of the shoulder joint by means of simulations and prototype testing.

The structure of this article is outlined as follows: Section II delineates the electromechanical configuration of the shoulder joint. Section III encompasses the elaboration of the kinematic model. Section IV displays the dynamic and empirical outcomes derived from real prototypes of the shoulder. The results obtained from the experiments are discussed and the proposed closed-loop kinematic chain is compared to other studies in Section V. Ultimately, Section VI introduces the summary of findings, along with prospects for forthcoming advancements.

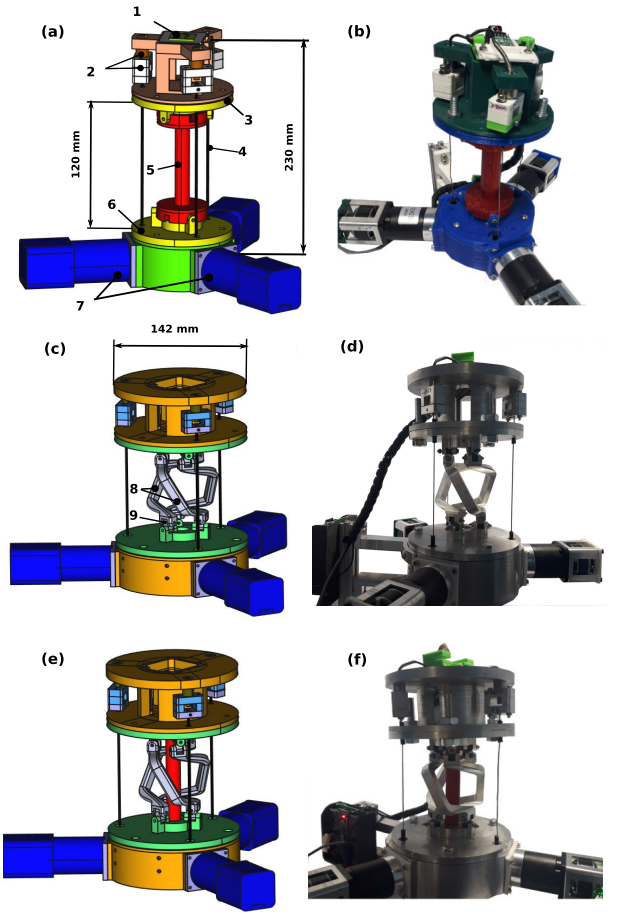

FIGURE 1. Assembled structures of the shoulder joint. a) CAD design of 1-F structure; b) Realistic view of 1-F structure; c) CAD model of 3-RRRR structure; d) Real prtototype of 3-RRRR; e) CAD version of 3-RRRR-1-F prototype; f) Physically assembled 3-RRRR-1-F prototype. 1-Inertial measurement unit (Model: AltIMU-10 v5); 2-Force sensor with a holder; 3 - Platform part; 4 - Tendon line; 5 - TPU based elastic central limb; 6-Base part; 7-Assembled servomotors; 8-rigid limbs; 9-Universal joint.

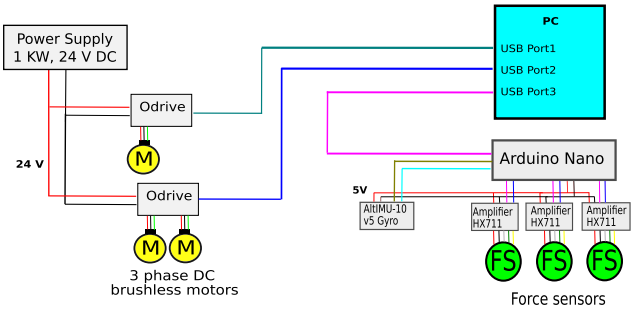

FIGURE 2. Electrical circuit of the shoulder joint prototype.

II. ELECTROMECHANICAL DESIGN

An incremental design approach was employed to finalize the development of the proposed shoulder joint, which consists of three lateral rigid limbs and a central elastic limb.

Initially, a prototype featuring only the central elastic limb was tested independently (see Figs. 1a and 1b) [41]. In this case, the shoulder joint (1-F structure) features a

TPU-based flexible central limb with bending capability, which serves also as a connection between the base and the moving platform. Subsequently, a prototype with three lateral rigid limbs (3-RRRR structure) [1], [33] was realized (refer to Figs. 1c and 1d) and subjected to testing. Finally, these two configurations were integrated to form the proposed architecture (3-RRRR-1-F structure) see Figs. 1e and 1f, which was then studied in detail. As a result, three distinct prototypes for the shoulder joint, as shown in Fig. 1, were designed using FreeCAD software and realized using CNC and 3D printing techniques.

In terms of actuation, all shoulder joint prototypes are driven by three tendons positioned 120 degrees apart from one another. The tendons are connected to Brushless Direct Current (BLDC) servomotors installed at the base of the joint, which are arranged perpendicular to their respective tendon lines thanks to the usage of pulleys. To gauge the tension applied to each tendon line, a force sensor is attached between the tendon line and the rotating platform. Additionally, an IMU sensor was installed on top of the moving platform to measure its orientation in terms of roll, pitch, and yaw angles.

Various electronic components were utilized for driving the servomotors and controlling the configuration of the shoulder joint (as depicted in Fig. 2). The DC power supply unit, with 24 V nominal, provides electrical power to the two motor controllers (Model: ODrive 3.5), where each motor controller has the capability to command two motors simultaneously and communicates with a Linux OS based PC, which runs Python scripts. Two USB ports of the PC are connected to the motor controllers, while a third USB port is attached to an Atmega-328 micro-controller.

For measuring the tension in the tendons, load cells are employed. Their output signals are enhanced using instrumentation amplifiers (Model: HX711). To allow the operator to control and monitor the shoulder joint prototype, the sensory signals are acquired by the micro-controller with a frequency of 100 Hz.

Initially, the calibration of the three force sensors and the IMU sensor was performed. They were subsequently linked to the micro-controller. In order to reduce the length of spare cables and minimize the noise, a motherboard with soldered pins and shielded cables was developed to make a bridge connector between the micro-controller and sensors. In order to avoid short circuits, all components that hold the electrical boards and cables were fabricated from plastic material.

A. ELASTIC CENTRAL LIMB (1-F) STRUCTURE

The design of the central limb was developed to meet specific criteria, which encompass the following key requirements: 1) Ensuring there is no collision between the links, tendon lines, platform, and base; 2) Allowing bending of the limbs while restricting torsion, as referenced by [41]; 3) Deliberately considering the shape, density, and geometry of the central limb to prevent breakage and deformation when subjected to high stress from in-house-assembled powerful servo motors [41], [42] with an average mechanical power of 200 W each, operating at 40-60% efficiency.

TABLE 1. Bending over twisting ratios. Defining the highest permissible magnitude of displacement for a TPU based central limb structure under various thicknesses and applied forces.

		Applied force, N (σ=60 MPa, H=134 mm)			
		30	60	90	120
Width, h	12 mm	28 mm/27 mm	56 mm/53 mm	83 mm/80 mm	111 mm/107 mm
	15 mm	12 mm/11 mm	24 mm/22 mm	36 mm/33 mm	48 mm/44 mm
	18 mm	6.4 mm/5.6 mm	13 mm/11.2 mm	19 mm/17 mm	26 mm/22.5 mm

The TPU-based central limb's displacement (in mm) was examined through Finite Element Analysis (FEA) by applying 60 N force at various thicknesses and heights under two distinct scenarios (Fig. 3): 1) Bending and 2) Twisting. Generally, as the elastic material gets longer and thinner, it will be much easier to bend and twist it.

Additionally, Table 1 provides a visual representation of the methodology used to achieve an optimized design for the elastic element. The table presents the outcomes of displacement magnitude for various diameters and applied external forces while maintaining a constant height during the testing. The target was to minimize the torsion and get a higher displacement magnitude during the bending process. In other words, bending at lower applied force was preferable in order to reduce the energy consumption to pull the tendon line. Also, the torsion about the yaw orientation is unwanted due to the fact that it cannot be controlled by the tendon lines, thus it must be minimized. Three different thickness configurations for the central limb were examined (see Table 1): 1) 12 mm; 2) 15 mm; 3) 18 mm. External forces ranging from 30 N to 120 N were employed to test the bending and twisting behaviors of the TPU limb. As the limb's diameter increases by 20-25%, both its bending and twisting displacements decrease by half. For a 12 mm width structure with a 30 N external force, bending and torsional magnitudes closely align. However, for a 18 mm thickness model, the torsional magnitude displaces to 5.6 mm, approximately 15% lower than the bending magnitude. Interestingly, the amount of external force growth is almost linearly proportional to the amount of bending and twisting magnitude growth. Consequently, the most suitable geometry for the proposed central limb, with an elasticity of 60 MPa, is determined by a thickness (h) of 15 mm and a height (H) of 134 mm (see highlighted green colored data in Table 1).

B. RIGID LIMB (3-RRRR) STRUCTURE

Three aluminum-based rigid limbs are connected between the base and platform, where each limb contains one limb attached to one universal joint from the bottom and one universal joint from top part [33], see Figs. 1c and 1d. The configuration of each rigid limb is not located vertically straight when the shoulder joint is in the home position. Instead, the limb configurations are vertically curved.

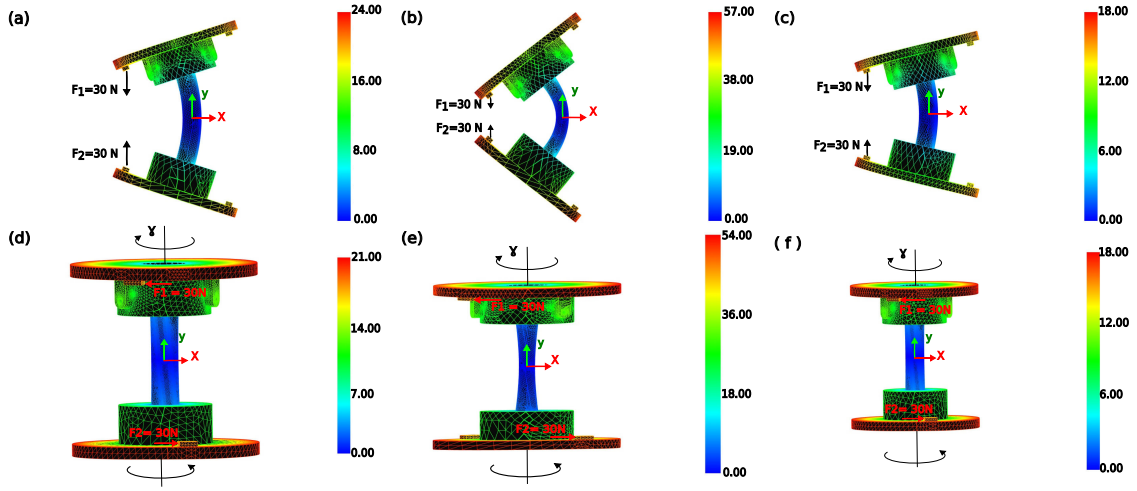

FIGURE 3. In this bending and twisting plan, we analyzed how the magnitudes of displacement (measured in millimeters) varied with a method of FEA when different geometries of the central limb, made from TPU material, are subjected to a consistent applied external force of 60 Newtons. These geometries are as follows: a,d) h = 15 mm; H = 134 mm; b,e) h = 12 mm; H = 134 mm c,f) h = 15 mm; H = 118 mm.

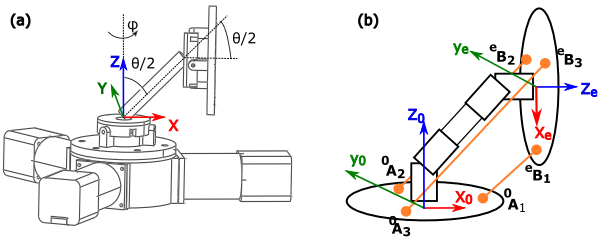

FIGURE 4. (a) Sketch of the equivalent kinematic model of the proposed parallel manipulator with the moving platform bended about the roll axis at a maximum angle. (b) Tendon attachment points.

One of the major challenges is minimizing mechanical backlash, which can be addressed by securing the universal joints tightly to the links, platform, and base of the mechanism. Failure to do so may cause the platform to twist, resulting in the end-effector frame losing its configuration.

Furthermore, friction should be minimized by smoothing out the surfaces of the base, platform, universal joints, and solid limbs to eliminate any roughness.

C. HYBRID LIMB (3-RRRR-1-F) STRUCTURE

The target configuration of hybrid limbs (Figs. 1e and 1f) works in the same principle as that of TPU and rigid limbs based model. It is important to limit the thickness of the TPU component in order to prevent it from colliding with the rigid limbs as the platform bends in roll and pitch directions. In this case, the TPU limb with 15 mm thickness obtained as an optimum design from Table 1 is sufficient. Otherwise, the distance between the rigid legs must be significantly increased.

More details about the hybrid limb design will be explained in the following sections because it has some advantages compared to the other two models in terms of dynamic behavior.

III. KINEMATIC MODEL

In this work, the kinematics of the shoulder joint is described by using two primary frames. The reference frame is displaced on the fixed base, while the relative frame is rigidly attached to the moving platform, see Fig. 4b. The relative motion between these two frames can be modeled by a single central limb consisting of two universal joints connected in series (4 DOFs). However, due to the presence of the three lateral rigid limbs, the motion of the central limb is constrained to two DOFs, a bending angle θ, and a bending direction ϕ. Fig. 4a demonstrates a sketch of the shoulder joint bent at a 90-degree angle about the roll axis.

A. DIRECT AND INVERSE KINEMATICS

Assuming that the base and moving platform can be modeled in the form of a triangular structure with equal sides, the height of the parallel manipulator in the home position is 120 mm, which corresponds to the lengths of the three tendon lines. The tendon lines connect the base to the platform by being attached to the edges of the triangles.

Overall, the kinematic representation of the shoulder joint comprises eight frames, as depicted in Fig. 5, row 1. Frames 0, 1, 2, and 3 are located on the fixed base part, which is static. Frame 4 can rotate in the pitch or roll directions and is linked to frame 5 through link l_{45} that has 120 mm length. Similarly, frame 5 can rotate in the pitch or roll axes by regulating the platform orientation. Generally, the forward kinematics (FK) problem for a parallel manipulator is quite challenging, however, as indicated in [33], for a 2 DOFs parallel manipulator as shown in Fig. 5, it can be solved by considering a sequence of five transformations with respect

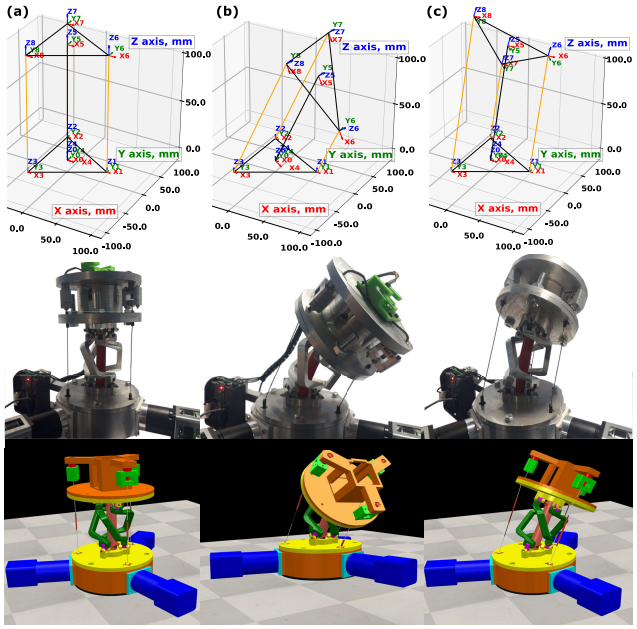

FIGURE 5. Geometrical model, actual setup, and simulation (CoppeliaSim software) of the shoulder joint consisting of three lateral rigid limbs and a central elastic limb (3-RRRR-1-F structure). Samples of the platform orientation in terms of: a) maintaining in a home position; b) performing a 60-degree roll axis rotation; c) executing a −45-degree pitch axis rotation.

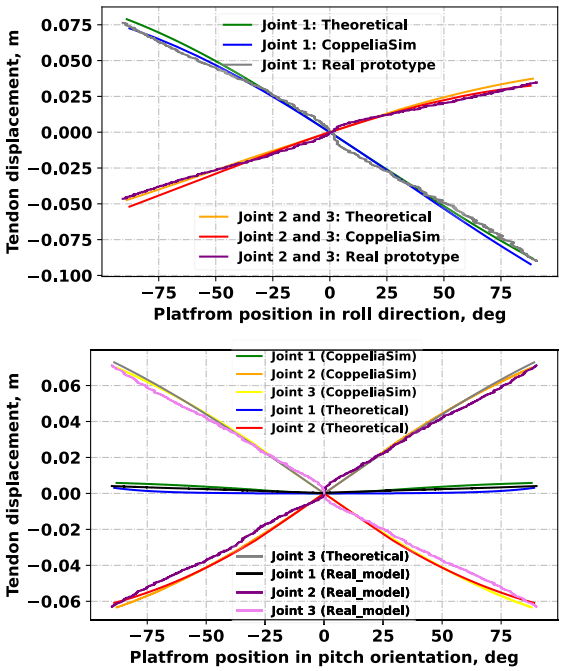

FIGURE 6. The findings of the platform's movement in the roll and pitch axes are presented for a novel hybrid parallel manipulator featuring three tendon lines. A comparison is made between the results obtained from the numerical solution, the CoppeliaSim model, and the physical setup of the proposed shoulder joint.

to the moving frame. We start with a rotation of an angle ϕ about the z axis, this defines the direction of the bending plane. Then we rotate about the y-axis of $\theta/2$, we translate along the z-axis of a distance h, and rotate again of $\theta/2$ about the y-axis. Finally, to fulfill the constraints imposed by the three lateral limb, we rotate of an angle -ϕ about the z-axis. By using the post-multiplication rule, we obtain the compound homogeneous transformation as in Eq. 1:

$$
\begin{aligned}
&{}^{0}\mathrm{T}_{e} \\
&= R_z(\phi)R_y(\frac{\theta}{2})T_z(h)R_y(\frac{\theta}{2})R_z(-\phi) \\
&= \begin{bmatrix}
1-2c^2(\phi)s^2(\frac{\theta}{2}) & -s(2\phi)s^2(\frac{\theta}{2}) & c(\phi)s(\theta) & hc(\phi)s(\frac{\theta}{2}) \\
-s(2\phi)s^2(\frac{\theta}{2}) & 1-2s^2(\phi)s^2(\frac{\theta}{2}) & s(\phi)s(\theta) & hs(\phi)s(\frac{\theta}{2}) \\
-c(\phi)s(\theta) & -s(\phi)s(\theta) & c(\theta) & hc(\frac{\theta}{2}) \\
0 & 0 & 0 & 1
\end{bmatrix}.
\end{aligned} \tag{1}
$$

The terms c(ϕ) and s(θ) are shorthand for cos(ϕ) and sin(θ) respectively. Subsequently, the positions of the frames 6, 7, and 8 situated at the edges of the platform (as shown in Fig. 5, row 1) can be determined by pre-multiplying their initial pose by ${}^{0}T_e$. If ${}^{0}A_i$ represents the position of the tendon-i attachment to the fixed base, and ${}^{e}B_i$ the position of the tendon-i attachment to the moving base with respect the moving reference systems, Eq.2 can be utilized to compute the distance of the cable line 1 from frame 1 to 6, the distance of the cable line 2 from frame 2 to 7 and the distance of the cable line 3 from frame 3 to 8, thus effectively solving the Inverse Kinematic (IK) problem.

$$
l_i = ||{}^{0}\mathrm{T}_{e}{}^{e}\mathrm{B}_i - {}^{0}\mathrm{A}_i|| \quad \text{for i = 1,2,3;} \quad l = \begin{bmatrix} l_1 & l_2 & l_3 \end{bmatrix}^T. \tag{2}
$$

The length of each cable line changes compared to the home position length l_h when the parallel manipulator bends and this amount of displacement is defined by deducting the reference length from the final cable length (Eq. 3).

$$
\Delta l_i = l_i - l_h \quad for \quad i = 1, .., 3. \tag{3}
$$

l_h - initial tendon length that corresponds to the distance between the base and moving platform in its home position. In the shoulder prototype, the rigid limbs, base and platform, are constructed from aluminum material to avoid bending and even breaking at higher tensions applied by the motors (as depicted in Fig. 5, row 2). In order to control the position of the servomotors, it is necessary to convert each tendon line displacement to the corresponding pulley's number of turns, where the pulley is attached to the actuator's shaft to wind the cable line. In other words, the BLDC motor's position is computed based on the tendon line displacement calculated from the theoretical result of Eq. 3 and the motor position as it is expressed in Eq. 4:

$$
a_i = \frac{\Delta l_i}{2 \cdot \pi \cdot R \cdot GR}. \tag{4}
$$

The variables used in the analysis of the Eq. 4 are as follows: a_i - number of turns of the motor i; Δl_i -displacement of the tendon line, mm; GR stands for the gear ratio of the motor set;

R - radius of the pulley soldered with the gearbox shaft used to wind the cable line, mm. The kinematic behavior of the shoulder joint (as seen in Fig. 5, row 3) was verified using the CoopeliaSim based model. The input to the simulation was the orientation of the platform, while the output was the positions of the prismatic joints that represents the cable lines.

The theoretical model was validated with both the simulation and the real shoulder prototype. The comparison is visualized in the plots of Fig. 6, which shows the relationship between the platform rotation in the roll and pitch axes and the corresponding tendon displacement.

During platform motion in the pitch direction, the first servo rotates slowly with a small tendon displacement, while the other servos exhibit symmetrical behavior with a higher tendon motion. Conversely, during the platform rotation in the roll axis, one servo rotates forward by pulling the platform, while the other two servos rotate backward by stretching the tendon lines uniformly.

The results from the three models, as shown in Fig. 6, closely align, particularly at low angles of pitch and roll rotations of the platform. This indicates that the behavior of the theoretical and CoppeliaSim models closely mimics the behavior of the shoulder joint prototype.

B. DIFFERENTIAL KINEMATICS ANALYSIS

The objective of this section is to determine the linear velocity of the tendon lines as a function of the target angular velocity about the pitch and roll axes. In order to relate these quantities, it is necessary to obtain the corresponding Jacobian matrix.

The transformation ${}^0T_e$ in Eq. 1 refers to the pose of the end-effector frame (moving platform) with respect to the reference frame. By considering the positional part of ${}^0T_e$ (last column) and taking the time derivative by using the chain rule, we can obtain the positional Jacobian matrix (with a size of 3×2) by collecting the coefficients of $\dot{\phi}$ and $\dot{\theta}$, Eq. 5:

$$J_{pos} = \begin{bmatrix} -hs(\phi)s\left(\frac{\theta}{2}\right) & \frac{hc(\phi)c\left(\frac{\theta}{2}\right)}{2} \\ hs\left(\frac{\theta}{2}\right)c(\phi) & \frac{hs(\phi)c\left(\frac{\theta}{2}\right)}{2} \\ 0 & -\frac{hs\left(\frac{\theta}{2}\right)}{2} \end{bmatrix}. \tag{5}$$

In other terms, by multiplying the positional Jacobian matrix with the angular velocities of the pitch and roll axes, the linear velocity of the end-effector frame can be computed as in Eq.6:

$$v = \begin{bmatrix} v_x & v_y & v_z \end{bmatrix}^T = J_{pos} \begin{bmatrix} \frac{d\phi}{dt} & \frac{d\theta}{dt} \end{bmatrix}^T. \tag{6}$$

To obtain the Jacobian that relates the angular velocity of the moving platform, expressed in the Cartesian space, and the velocity vector $[\dot{\phi},\ \dot{\theta}]^T$, we need to consider the first 3 columns of the matrix in Eq. 1 that represents the orientation of the moving platform, Eq. 7.

$$R = \begin{bmatrix} 1 - 2c^2(\phi)s^2(\frac{\theta}{2})) & -s(2\phi)s^2(\frac{\theta}{2}) & c(\phi)s(\theta) \\ -s(2\phi)s^2(\frac{\theta}{2}) & 1 - 2s^2(\phi)s^2(\frac{\theta}{2}) & s(\phi)s(\theta) \\ -c(\phi)s(\theta) & -s(\phi)s(\theta) & c(\theta) \end{bmatrix}. \tag{7}$$

The rotation matrix is then derived with respect to time to calculate the angular velocity matrix S as in Eq. 8 [43].

$$\frac{dR}{dt} = \begin{bmatrix} \frac{d(r11)}{dt} & \frac{d(r12)}{dt} & \frac{d(r13)}{dt} \\ \frac{d(r21)}{dt} & \frac{d(r22)}{dt} & \frac{d(r23)}{dt} \\ \frac{d(r31)}{dt} & \frac{d(r32)}{dt} & \frac{d(r33)}{dt} \end{bmatrix}, \quad S = \frac{dR}{dt}R^T. \tag{8}$$

Finally, the angular velocity vector can be obtained from the elements of the skew symmetric matrix S as in Eq. 9:

$$w = \begin{bmatrix} S(3,2) & S(1,3) & S(2,1) \end{bmatrix}^T. \tag{9}$$

Since the angular velocity can be written as the product of the orientational Jacobian matrix with the vector of angular velocities about the pitch and roll axes (Eq. 10).

$$\begin{bmatrix} w_x & w_y & w_z \end{bmatrix}^T = J_{orient} \begin{bmatrix} \frac{d\phi}{dt} & \frac{d\theta}{dt} \end{bmatrix}^T. \tag{10}$$

We can obtain the elements of the matrix J_{orient} by collecting the coefficients that multiply $\dot{\phi}$ and $\dot{\theta}$ in Eq. 11.

The complete 6×2 Jacobian matrix can be finally formulated by casting both the positional and orientational Jacobians into a single matrix, as in Eq. 11.

$$J_{orient} = \begin{bmatrix} -c(\phi)s(\theta) & -s(\phi) \\ -s(\phi)s(\theta) & c(\phi) \\ 1 - c(\phi) & 0 \end{bmatrix}, \ J = \begin{bmatrix} J_{pos} \\ J_{orient} \end{bmatrix}. \tag{11}$$

Finally, the moving platform's linear and angular velocities are computed as described in Eq.12.

$$\begin{bmatrix} v_x & v_y & v_z & w_x & w_y & w_z \end{bmatrix}^T = J \begin{bmatrix} \frac{d\phi}{dt} & \frac{d\theta}{dt} \end{bmatrix}^T. \tag{12}$$

Alternatively, it is possible to approximate the angular velocity in the yaw and roll axes when the end-effector velocities are provided as in Eq.13.

$$\begin{bmatrix} \frac{d\phi}{dt} & \frac{d\theta}{dt} \end{bmatrix}^T = J^+ \begin{bmatrix} v_x & v_y & v_z & w_x & w_y & w_z \end{bmatrix}^T, \tag{13}$$

where J^+ represents the pseudo inverse of the Jacobian matrix, in Eq. 14:

$$J^+ = \begin{bmatrix} -\frac{hc(\phi)c(\frac{\theta}{2})}{h^2c^2(\frac{\theta}{2})-2\ s(\theta)+2} & \frac{hc(\frac{\theta}{2})s(\phi)}{h^2c^2(\frac{\theta}{2})-2\ s(\theta)+2} & 0 \\ \frac{2hs(\phi)s(\frac{\theta}{2})}{h^2+4} & \frac{2hc(\phi)s(\frac{\theta}{2})}{h^2+4} & -\frac{2hc(\frac{\theta}{2})}{h^2+4} \\ -\frac{c(\theta)s(\phi)}{h^2c^2(\frac{\theta}{2})-2\ s(\theta)+2} & -\frac{c(\phi)c(\theta)}{h^2c^2(\frac{\theta}{2})-2\ s(\theta)+2} & \frac{1-s(\theta)}{h^2c^2(\frac{\theta}{2})-2\ s(\theta)+2} \\ -\frac{4c(\phi)}{h^2+4} & \frac{4s(\phi)}{h^2+4} & 0 \end{bmatrix} \tag{14}$$

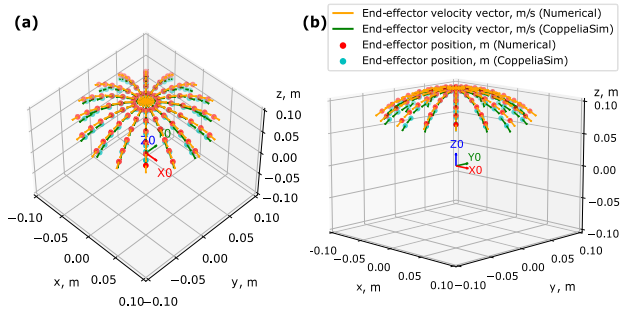

FIGURE 7. Kinematics and workspace of the proposed shoulder joint with position and velocity vectors of the end-effector frame at different projections. a) 3D view at elevation = 45 deg, azimuth = −45 deg and roll = 0; b) 3D view at elevation = 10 deg, azimuth = −45 deg and roll = 0.

Due to the fact that to control the velocity of the moving platform, the servo-motors must control the tendon velocities (joint velocities), it is necessary to derive an appropriate Jacobian that relates these quantities. The tendon displacements, see Eq. 2 left side, can be computed by subtracting the coordinates of the attachment points of the tendon lines to the fixed base, ${}^0A_i$, from the coordinates of the roto-translated attachment points to the moving platform ${}^0T_e^l B_i$.

We can derive the tendon velocities by calculating the time derivative of the components of the vector l, and collecting the coefficients that multiply $\dot{\phi}$ and $\dot{\theta}$ we obtain the Jacobian matrix J_j, which relates the vector of the angular velocities $[\dot{\phi},\ \dot{\theta}]^T$ with the linear velocities of the three tendon lines:

$$\left[\frac{dl_1}{dt}\quad \frac{dl_2}{dt}\quad \frac{dl_3}{dt}\right]^T = J_j \left[\frac{d\phi}{dt}\quad \frac{d\theta}{dt}\right]^T, \tag{15}$$

and substituting Eq. 13, we obtain Eq. 16:

$$\left[\frac{dl_1}{dt}\quad \frac{dl_2}{dt}\quad \frac{dl_3}{dt}\right]^T = J_j J^+ \left[v_x\quad v_y\quad v_z\quad w_x\quad w_y\quad w_z\right]^T, \tag{16}$$

where J_j refers to the Jacobian matrix related to the joint (or tendon) position.

It is important to note that, since the platform has only 2 DOFs controlled by three tendons, it is not possible to assign arbitrary linear and angular velocities in Eq.16.

The analysis of the end-effector's forward kinematics and workspace was tested and illustrated from both numerical and CoppeliaSim software outcomes as in Fig. 7. The numerical calculations were executed based on the previously mentioned equations, whereas the CoppeliaSim results were obtained from the simulation. We can observe that when the end-effector is near the home position, its positions and kinematic behaviors exhibit remarkable similarity in both the numerical and simulation models, as the platform strives to move horizontally. However, when the platform bends by ± 90 degrees in the roll or pitch axes, which represents the maximum bending angle, the position and velocity vector of the end-effector in the CoppeliaSim model tend to direct slightly downward in comparison to the numerical solution. The platform executes an elliptical motion, approximately resembling half of a hemisphere, with a height span of 3.5 cm and a diameter span of 17 cm.

Algorithm 1 Solving the Inverse Kinematics Problem for a CDPM Within a Reachable Range of Angles

Input: Input platform positions, θ, ϕ
Output: Motor positions, a_i, i=1,2,3
if $abs(\theta) > 90$ **then**
  $\theta = 0$ /* Motion forbidden */
end
for $i \longleftarrow 1$ *to* 3 **do**
  Solve Eq. (1) for ${}^0T_e$, given θ and ϕ.
  Calculate l_i from Eq. (2).
  Find the tendon displacement Δl_i from Eq.(3).
  Calculate the motor position a_i from Eq. (4)
    /* Considering the platform's reachable angles to avoid from link collisions */
  return a_i, i=1,2,3
end

Finally, the algorithm of the inverse kinematics solution (see Algorithm 1) was implemented in Python 3 including the motion range of the platform, which is limited to avoid from link collisions.

C. SINGULARITY ANALYSIS OF THE PARALLEL MANIPULATORS

Singularities in parallel manipulators arise when the system experiences a loss of degrees of freedom or becomes unmanageable in certain configurations. These situations can result in diminished rigidity, decreased accuracy, or even complete operational failure. In other words, presence of a singularity issue can cause the risk of losing the platform configuration. It is preferable to avoid singularity to control the closed-loop kinematic chain's platform precisely. In [44],the design of the SDelta parallel manipulator with a cuboid platform was optimized to achieve a desirable workspace free from singularities. Singularity equations specific to the symmetric 5-DOF 3-RRUR closed-loop kinematic chain were analyzed in [45]. In this study, the 3-RRRR and 3-RRRR-1-F kinematic structures share similar characteristics with the quaternion joint described in [33], where both mechanisms avoid singularity issues at a reachable workspace of the platform by incorporating two universal joints in each rigid limb.

To avoid singularities, the determinant of the product of the transposed and original Jacobian matrices is set to a non-zero value. This condition applies to both the positional Jacobian matrix J_{pos} and the orientational Jacobian matrix J_{orient}, as demonstrated in Eq. 17:

$$\det\left(J_{pos}^T J_{pos}\right) \neq 0 \quad and \quad \det\left(J_{orient}^T J_{orient}\right) \neq 0. \tag{17}$$

By combining the positional Jacobian matrices J_{pos} represented in Eqs. 5 and 17, the values for θ are defined as shown

TABLE 2. Comparing the results obtained from the first two experiments.

	Prototype		
Type of experiment	**Elastic limb (1-F)**	**Rigid limbs (3-RRRR)**	**Hybrid (3-RRRR-1-F)**
Single cable motion	Maximum 2.5 J system energy	N/A	Maximum 1.9 J system energy
Dynamic response and vibration attenuation	N/A	High vibration	Vibration minimized by 50%

in Eq. 18:

$$\det\left(J_{pos}^{T}J_{pos}\right)=\frac{h^{2}s^{2}(\frac{\theta}{2})}{4}\neq 0;\quad \theta\neq\pm 2\pi k,\ k\in Z. \tag{18}$$

Similarly, from the orientational Jacobian matrix term J_{orient} given in Eqs. 11 and 17, the values for θ and ϕ are specified in Eq. 19:

$$\det\left(J_{orient}^{T}J_{orient}\right)=s^{2}\theta+(1-c\phi)^{2}\neq 0, \tag{19}$$

where $\theta\neq\pm\pi k,\ k\in Z$ and $\phi\neq\pm 2\pi n,\ n\in Z$. In this case, Z refers to integers.

Consequently, it is demonstrated that the singularities lie outside the platform's reachable regions.

IV. EXPERIMENTAL RESULTS AND COMPARISONS

This section presents three different experiments. The first two focus on testing the platform's rotation in the roll direction and analyzing energy storage and dynamic response, considering all three kinematic architectures. To minimize the influence of the control system on the measured quantities, only one of the three tendons was activated. Additionally, since the 3-RRRR configuration lacks an elastic element and cannot store energy, the corresponding energy storage experiment was omitted for this prototype (see Table 2). Similarly, due to distortion of the TPU element that causes error generation at the platform orientation in the 1-F prototype, no dynamic response experiment was conducted. In the last experiment, only the stiffness of the 3-RRRR-1-F prototype is evaluated, considering it an optimal design based on the outcomes of the previous experiments.

A. SINGLE TENDON MOTION TESTING

The goal of this section is to characterise the physical behavior of the elastic central limb, while a motor, with variable velocities, pulls and releases the platform through the cable line in roll direction. Meanwhile, the other two motors remain inactive with fully extended cables, offering no resistance to the active actuator. Additionally, the cable-driven parallel manipulators (CDPMs) are positioned in a vertical orientation. (see Fig. 1).

1) SINGLE ELASTIC CENTRAL LIMB SHOULDER JOINT 1-F STRUCTURE

To evaluate the dynamic behavior of the shoulder joint, we performed different rotational motions while measuring the forces involved. An actuator with a gear ratio of 1:15 pulling the platform in roll direction by 6 cm tendon displacement was tested at 2 different velocities: a) medium-velocity-motion with an average of 2.4 cm/s for the tendon velocity; b) slow-velocity-motion, averaging 0.6 cm/s tendon velocity (Fig. 8b). The velocities are represented as set-points in the graphs, which are continuous without dropping at the end.

During the experiments, the following quantities were measured: 1) force readings from the force sensor installed in series with each tendon line; 2) motor position derived from the encoder; 3) motor current and voltage measurements taken from the motor board.

As it is possible to see from the plot of Fig. 8a, the force vs displacement characteristic presents a hysteresis, typical of elastic materials. At a higher velocity, the curvature of the force is slightly shifted to the leftward compared to the case with lower actuator velocity. This means, as the force sensor is pulled quickly by the cable line, the amount of applied force increases rapidly by reaching the final value. During the pulling process, the TPU-based central limb counteracts the actuator's motion by demanding a higher amount of force, this is confirmed by the computation of the mechanical and electrical power (Fig. 8a, 8c, and 8d). On the other hand, the actuator can easily release the tendon line because the TPU based central limb tries to come back to its home position by assisting the motor to rotate in the backward direction. This phenomenon resembles the experience of ascending and descending stairs, with upward movement requiring more effort due to gravity. Similarly, bending the TPU sample is harder than releasing it because it has a resistive internal force that creates the phenomenon of hysteresis.

In addition, as the platform is made of plastic material that weights about 250 grams (see Figs. 1a and 1b), its gravitational force is negligible, if compared to the resistive force of the central elastic limb measured along the cable (Fig. 8a).

The tendon's angular velocity (deg/s) was computed by differentiating the motor position (deg) obtained from the encoder. Also, the tendon displacement was obtained from the actuator position (Eq. 4). Both current and tendon's angular velocity were filtered to suppress the noise before computing the tendon's linear velocity (cm/s). The results of measured data within each 4-5 time samples were averaged with a filter.

The dynamic quantities of the servomotor were computed as in Eqs. 20 and 21.

$$T_{mech}=F\cdot R,\quad T_{electrical}=\frac{I\cdot V\cdot 60}{2\cdot\pi\cdot\omega}. \tag{20}$$

$$P_{mech}=\frac{T_{mech}\cdot\omega\cdot 2\cdot\pi}{60},\quad P_{electrical}=I\cdot V. \tag{21}$$

where F -force of the tendon line applied through the actuator, N; R- Radius of the gearbox pulley ($R=1$ cm); I - motor's current, A; V - motor's Voltage, V; ω - motor's angular velocity, rpm.

The aforementioned cycle was repeated for the forward and reverse rotation. On the horizontal axis of Fig. 8, we can

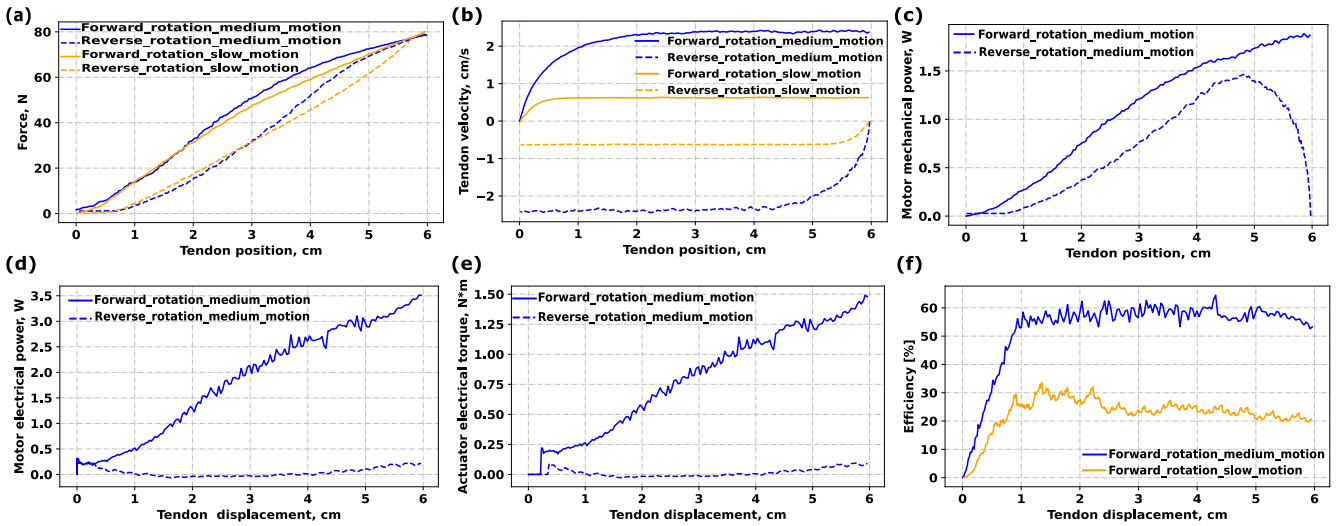

FIGURE 8. Actuation system dynamics with a TPU limb (1-F) based shoulder joint.

observe that both the tendon position and displacement increase when the actuator pulls the tendon line. On the other hand, the tendon position drops when the actuator releases the tendon line rotating in reverse direction, but the value of the tendon displacement grows during the actuator's releasing process. Finally, we can calculate the motor efficiency η as the ratio of mechanical energy to electrical energy.

The outcomes of this experiment revealed a substantial increase in the actuator efficiency, reaching up to 53%, during medium rotations with an average tendon velocity of 2.4 cm/s. In contrast, the efficiency during the slow motion, with an average tendon velocity of 0.8 cm/s, was twice lower (Fig. 8f).

2) PROTOTYPE WITH RIGID LIMBS (3-RRRR)

The rigid limbs of the 3-RRRR structure do not resist the motor as it pulls the platform, due to lack of elasticity and energy storage capacity. Additionally, the platform is 5-6 times heavier than that of the 1-F structure, thus the bending platform assists the motor by adding its load. Consequently, in the vertically oriented parallel manipulator (PM), the forces measured along the cables of the 3-RRRR prototype are minimal, making it difficult to calculate motor torque, power, or efficiency during cable pulling or extension. But the condition would be different when the PM is located in horizontal configuration because the platfrom load could resist against the pulling motor depending on the actuator location.

Although, slight friction exists in the joints of the rigid limbs while the platform is bending, the friction force is negligible compared to the gravitational force acting on the rotating platform. In other terms, the friction force produced in the solid limbs is unable to oppose the weight exerted by the aluminum platform when the motor pulls the tendon line.

3) HYBRID LIMBS BASED SHOULDER JOINT (3-RRRR-1-F STRUCTURE)

For the hybrid limbs based shoulder joint, the same experiment was performed as for the single elastic central limb prototype. However, compared to 1-F structure experiment, the following differences must be considered in terms of geometry, structure and materials (see Fig.1): 1) Higher platform workspace and base diameter; 2) Integrated 3 lateral rigid limbs; 3) Aluminum based platform with a weight of 1.5 kg. In addition, due to increased platform diameter and distance between the cables at 3-RRRR-1-F structure, the platform rotation can reach the maximum angle in roll direction by being perpendicular to the base part, which corresponds to 8 cm tendon displacement. Furthermore, the shoulder prototype integrates three motors with a gear ratio of 1:100 and the tendons are controlled at two different velocities: 0.6 cm/s and 6 cm/s.

As it is possible to evince from Fig. 9a, for the direct rotation, the force increases almost linearly. The maximum force value is approximately 66 N, slightly lower than that of the single elastic central limb prototype. The reason for that is integration of an aluminum platform that reduces the resistive force of the central elastic element. During the reverse rotation, the motor easily releases the tendon line by showing a curved graph. Overall, a kind of hysteresis is detected in the required force due to the fact that in the reverse rotation, the elastic central limb releases the potential energy accumulated during the forward motion.

The efficiency of the pulling actuator during the fast motion approaches to 95% at maximum bending angle (Fig. 9f), which is twice as high with respect to a slow actuator motion.

As the actuator pulls the cable, the total energy of the system increases. Interestingly, when the actuator rotates slowly and moves the tendon line at a velocity of 0.6 cm/s,

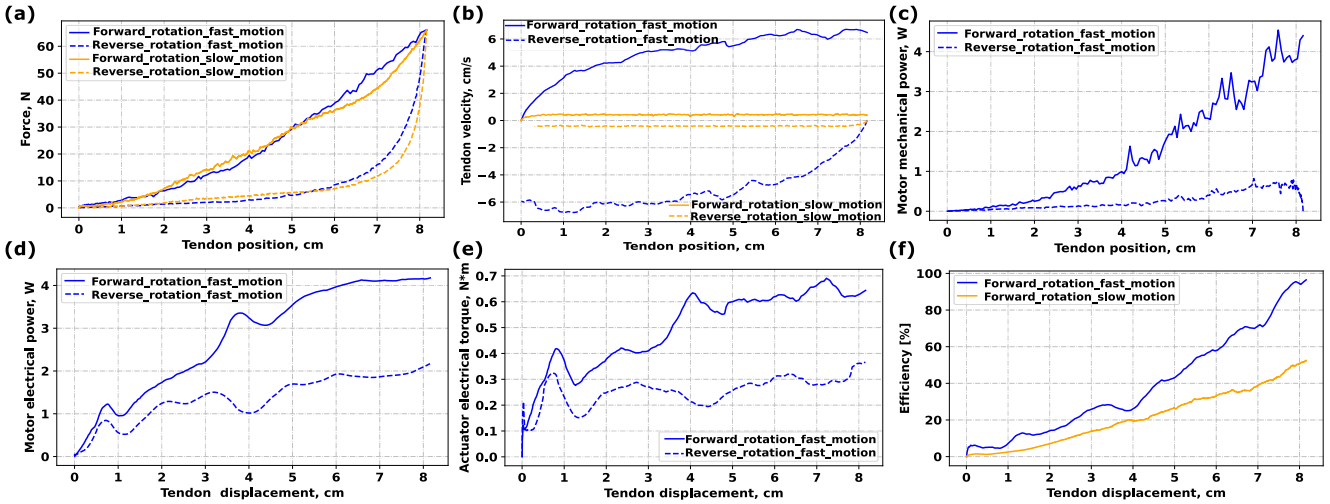

FIGURE 9. Actuation system dynamics with a hybrid limbs (3-RRRR-1-F) based shoulder joint.

the maximum system energy in the 1-F structure reaches 2.5 J, which is 20-25% higher than in the 3-RRRR-1-F prototype, due to the lightweight design of the platform at 1-F prototype (see bold lines Fig. 10). During the extension of the tendon line, the total system energy decreases as both the platform and cable return to their home positions that refers to the stored energy (see dashed lines Fig. 10). In this case, while slackening scenario of the tendon line and taking the dissipated energy E_{dis} into account, the maximum amount of stored energy for the 1-F and 3-RRRR-1-F structures exhibits 1.8 J and 0.7 J, respectively.

At a certain point along the tendon line position, the difference in total system energy between the pulling (forward rotation) and releasing (reverse rotation) process refers to the dissipated energy E_{dis} (see Fig. 10). In other words, as the platform bends with a tendon line being pulled by an actuator, E_{dis} term is nullified (refer to Eq. 22). Conversely, during the slackening process of the tendon line, the amount of dissipated energy E_{dis} is considered, which is subtracted from the total system energy of the pulling process.

$$E_{total} = E_{TPU} - E_{dis} \pm E_{platform} \pm E_{external} + E_{c.cab}. \quad (22)$$

Eq. 22 is the general expression to exhibit the amount of total energy of the system E_{total} that is spent to bend the platform by pulling a tendon line with a motor, including the deformation of the TPU element and the minor friction forces observed at the rigid limbs. Other terms in Eq. 22 are characterised as it follows: E_{TPU} - energy of the resistive elastic TPU element, J; E_{dis} - dissipated energy due to deformation, friction and internal resistance of the system, J; $E_{platform}$ - potential energy generated by weight of the platform, J; $E_{external}$ - external load energy applied on platform, J; $E_{c.cab}$ - amount of resistive energy against the platform rotation that is generated by counter cables, J. When the platform weight and external load counteract the pulling motor by supporting the elastic element, the signs for

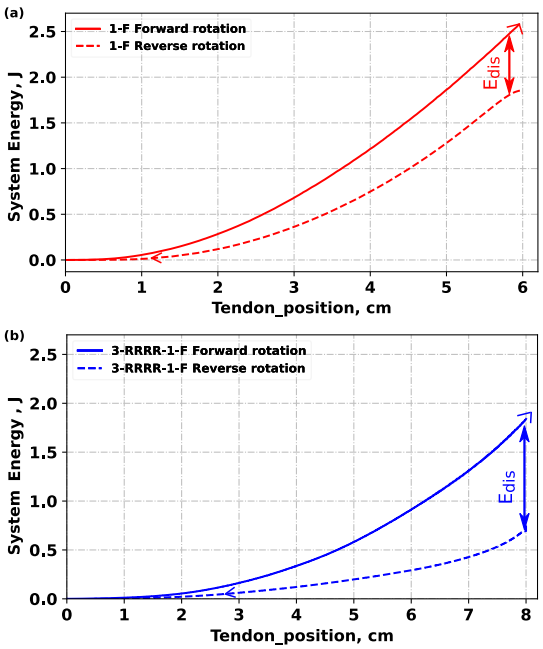

FIGURE 10. Comparing the total energy diagrams of the system at a slow platform velocity during the loading and unloading phases, with a single tendon line in the roll direction for closed-loop kinematic chains: a) 1-F structure; b) 3-RRRR-1-F structure.

$E_{platform}$ and $E_{external}$ can become positive, which means that the tension applied on the cable increases the accumulated total energy E_{total}. This phenomenon can happen when the CDPM is installed in horizontal orientation.

On the other hand, the signs for $E_{platform}$ and $E_{external}$ will be negative, if the CDPM is installed in vertical orientation. In this scenario, when the motor pulls the platform, the platform's weight aids the pulling motor by resisting the central elastic element.

In this experiment, both $E_{external}$ and $E_{c.cab}$ terms are negligible because there is no external load and the opposing cables are loosely attached to the platform. From Eq. 22, E_{total} mostly depends on E_{dis}, E_{TPU} and $E_{platform}$ terms. In Fig. 10a, a portion of the energy, up to a maximum of 0.7 J, is lost due to the deformation of the TPU limb in the 1-F structure. However, the amount of dissipated energy in the 3-RRRR-1-F prototype is twice as high as in the 1-F structure Fig. 10b, due to additional energy loss from the deformation of the TPU element caused by the aluminum platform and frictional forces between the rigid limbs. The potential energy of the platform load $E_{platform}$ is based on the mass, height h and bending angle θ of the platform (Eq. 23).

$$E_{platform} = m \cdot g \cdot h \cdot sin(\frac{\theta}{2}),\ E_{total} = E_{mech} = \sum_{i=1}^{i_{max}} P_i \Delta t. \tag{23}$$

Alternatively to Eq. 22, the amount of total energy in the shoulder joint E_{total} can be calculated by integrating the mechanical power (refer to Eq. 23). In this case, for each sample i, the sample time Δt is multiplied by the mechanical power P_{mech} calculated from Eq. 21. The energies from the first iteration until the last one i_{max} are then summed, and the resulting graphs are shown in Fig. 10.

B. DYNAMIC RESPONSE AND VIBRATION ATTENUATION

To understand how the central elastic element affects the dynamic behavior of the hybrid limbs in the 3-RRRR-1-F shoulder joint, we conducted an experiment in which a disturbance force was applied to the moving platform. For this experiment, an additional force sensor was installed on the distal part of the moving platform to measure the disturbance force, while an IMU sensor was used to measure the platform's orientations. The tendons were tensioned, and the external force was applied to the platform in a direction orthogonal to the tendons. Consequently, the control system that regulates tendon tension is not affected by this torsional force. From a vibration analysis, both single TPU limbs, three rigid limbs and hybrid limbs models were installed in a horizontal configuration and they were compared according to the resistance against the external force applied to twist and bend the platform (Fig. 11). While the bending force F_2 was applied, the TPU 1-F-based model lost stability along the F_3 direction due to the absence of support from rigid limbs. (Fig. 11)a. This occurs because the elastic TPU element deforms under compression when each tendon line is pulled by a corresponding actuator with a constant force F_1. In contrast, the rigid limbs of the 3-RRRR structure do not deform because the solid legs lack elasticity. The platform remains in its home position without displacement, even when the tendon lines compress the rigid limbs through the platform. However, significant torsional backlash was observed in the home position, despite the solid limbs and universal joints being firmly connected to each other. (Fig. 12).

The two shoulder joint setups were compared in terms of vibration absorption and backlash (see Figs. 11b and 11c).

Results showed that the parallel manipulator 3-RRRR-1-F with the hybrid limb, in comparison to the pure rigid structure 3-RRRR, is able to absorb the vibration and minimizes the platform's twisting angle. With an external force of 4 N, the platform exhibited twisting of $\pm$ 1.5 degrees in the absence of the central flexible limb, while these maximum and minimum angles reduced when integrating the central elastic limb (Fig. 12a and 12d). When the external forces increased to 8N and 16N, the total angle of torsion grew to about $\pm$ 2 degrees and $\pm$ 4 degrees respectively. Overall, by introducing the central elastic limbs, the first pick of the oscillation was reduced of 40% when applying 4 N and 8 N and 20% when applying 16 N (see Fig. 12).

C. STIFFNESS ANALYSIS

In the previous experiments, the hybrid limbs (3-RRRR-1-F) structure outperformed both 3-RRRR and 1-F prototypes (refer to Table 2). As a result, in this section, the stiffness analysis is carried out only for the 3-RRRR-1-F prototype. The integration of an elastic central limb within the 3-RRRR-1-F structure has the effect to shape the stiffness of the shoulder joint. In order to measure the stiffness of the moving platform, an experiment was conducted, while bending the platform in different directions, the displacement and forces applied by the tendons were measured at vertically installed CDPM. This allowed us to estimate the stiffness of the platform expressed in the joint-space. As a second step, in order to map the stiffness to the Cartesian space, the Jacobian matrix of Eq. 16 was used, which relates the velocity in the joint space (i.e. tendons linear velocity) with the velocity of the platform in the Cartesian space.

In this analysis, only the positional part of the Cartesian-based Jacobian is considered to simplify the computation. Thus, the Cartesian based Jacobian matrix $J_C = J_J J^+$, which is used in Eq. 16, with dimension 3×6, is simplified to the form of J_{Cp} that has a dimension 3×3. By taking the transpose of this matrix we can write Eq. 24, which relates the static force applied to the tendons to the Cartesian force F applied to the moving platform.

$$\begin{bmatrix} F_x & F_y & F_z \end{bmatrix}^T = (J_{Cp})^T \begin{bmatrix} f_1 & f_2 & f_3 \end{bmatrix}^T. \tag{24}$$

The joint-i stiffness is found as the ratio of force to tendon displacement (Eq. 25):

$$k_i = \Delta f_i / \Delta l_i \qquad \text{for } i = 1,2,3. \tag{25}$$

The general representation of tendon force can be expressed by modeling it as a mass-spring-damper system (Eq.26):

$$f = k\Delta l + bv + ma. \tag{26}$$

However, as the motion of the platform in this experiment was very slow, the velocity and accelerations term can be neglected as first approximation, thus, using Eq. 25,

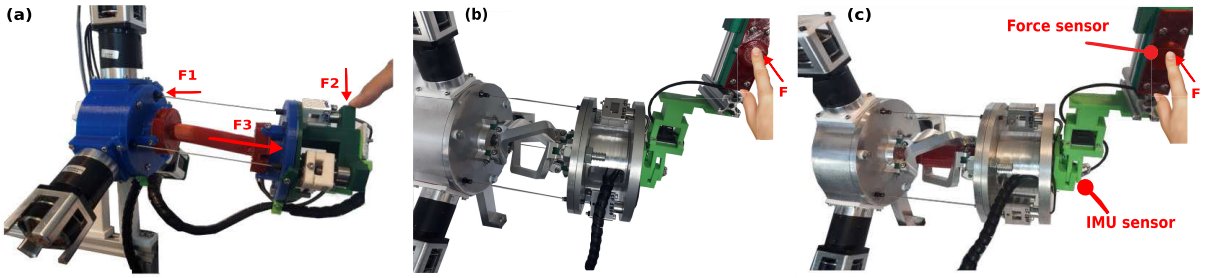

FIGURE 11. Realistic setup of the CDPM in horizontal direction. a) Single-limb TPU based version (1-F structure); b) Rigid limb based version (3-RRRR structure); c) Hybrid limbs based version (3-RRRR-1-F structure).

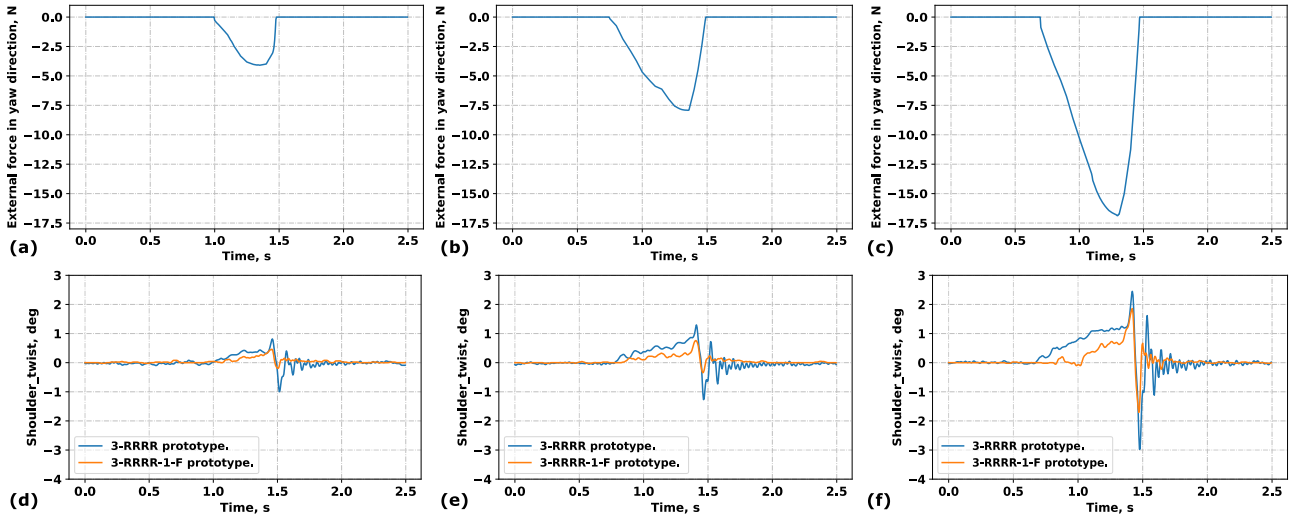

FIGURE 12. Testing the twisting angle and vibrations of the CDPM at variable applied torsional forces with a rigid central limb structure vs hybrid limb model. a, d) External load 4N; b, e) External load 8N; c, f) External load 8N.

we can calculate the value of the stiffness in different joint configurations (tendon positions).

After computing the joint stiffness from Eq. 25, the end-effector's stiffness matrix can be arranged by taking the diagonal stiffness matrix of the joints and Cartesian based Jacobians into account as in Eq. 27 [12], [46], [47]:

$$K_c = \begin{bmatrix} K_{xx} & K_{xy} & K_{xz} \\ K_{yx} & K_{yy} & K_{yz} \\ K_{zx} & K_{zy} & K_{zz} \end{bmatrix} = J_{Cp}^T \begin{bmatrix} k_1 & 0 & 0 \\ 0 & k_2 & 0 \\ 0 & 0 & k_3 \end{bmatrix} J_{Cp}. \quad (27)$$

Where the terms K_{xx}, K_{yy} and K_{zz} correspond to the stiffness along the x, y, and z directions respectively. We can represent these three components as a function of the angular position of the platform expressed as $[\phi,\ \theta]^T$, see Fig. 13 a-b.

To calculate the stiffness of the entire system, the procedure begins with the computation from Eq. 1 and concludes with Eq. 27. as demonstrated in Algorithm 2.

The plots in Fig. 13 report the calculated Cartesian stiffness together with the measured joint stiffness. As the structure of the shoulder joint has three tendon lines, the stiffness behavior is not symmetric. On the other hand, if there were four tendon lines in the parallel manipulator, it would be possible to get a symmetric shape of stiffness in the graphs. In other words, when the platform rotates in roll direction, the platform tends to have increased stiffness in x direction. Conversely, in pitch direction, the stiffness in y axis exhibits a dramatic increase. Generally, the stiffness of the end-effector in the z-direction increases for both roll and pitch orientations.

When the first servomotor pulls the tendon line, the other two actuators release. In this scenario, the stiffness of the first joint rises, while the symmetrically positioned other joints experience a significant decrease (see Fig. 13a). Consequently, only the first joint directly influences the platform's movement in the roll direction. Conversely, during platform motion in the pitch orientation (see Fig.13b), the stiffness of the third and first joints increases significantly. Simultaneously, the second servomotor, with reduced stiffness, allows slackening of the tendon line. As the platform's position in the pitch direction is situated between the first and third joints, these servomotors exert pulling forces on both sides of the platform. Consequently, tensions applied to the cables of the first and third actuators increase in proportion to the stiffness growth. Notably, when the platform angle exceeds 75 degrees in both roll and pitch

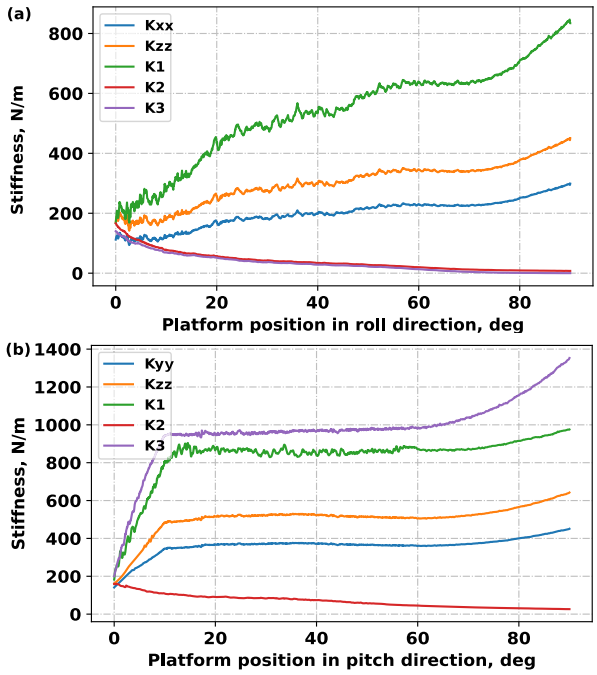

FIGURE 13. Analyzing the stiffness of the shoulder joint in 2 dimensional space. The graphs represent the stiffness vs angular position of end-effector in a) roll direction; b) pitch orientation.

Algorithm 2 Computation of the CDPM Stiffness Based on the Joint and Cartesian Spaces

Input: Input platform positions, θ, ϕ; Input cable tensions f_i, i=1,2,3
Output: Stiffness parameters, K_{xx}, K_{yy}, K_{zz}, k_i, i=1,2,3
if $abs(\theta) > 90$ *and* $abs(\theta) < -90$, **then**
  $\theta = 0$ /* Motion forbidden */
end
if $abs(\theta) \in [-90; 90]$, **then**
  Solve Eq. (1) and derive the last column elements for ${}^0T_e$ with dt to get v_x,v_y and v_z, given θ and ϕ.
  Calculate l_i from Eq. (2), i=1,2,3
  Derive the tendon displacement Δl_i from Eq. (3) with dt
  Measure ω_x, ω_y and ω_z with an IMU sensor
  Calculate $J_j J^+$ from Eq. (16) and convert to J_c /* Cartesian based Jacobian matrix */
  Compute the end-effector forces F_x, F_y and F_z from Eq. 24, given f_i, i=1,2,3
  Define the joint stiffness k_i from Eq. 25, i=1,2,3
  Solve Eq. (27) for K_{xx}, K_{yy} and K_{zz}
end

directions, the tension applied to the cables increases, while cable displacement decreases. This leads to a rapid growth in stiffness across all pulling joints and end-effector frames.

V. DISCUSSION

Based on the research works presented in Table 3, closed-loop kinematic chain structures can be categorized by factors such as platform rotation, displacement, number of actuators, central limb design, and the presence of cables. Notably, the types of central limbs vary, including those made solely of rigid limbs [1], [11], [12], [16], [22], [32], [33], [34], elastic structures [13], [14], [19], [28], [41], and hybrid forms [29], [30]. Only a few CDPM mechanisms feature hybrid structures, such as the combination of flexible spring with a sliding rigid limb [20] or flexible spring with three rigid legs [21]. There remains an opportunity to explore a CDPM with a hybrid structure that incorporates a central TPU element with bending capability and 3-RRRR rigid limbs. Although the closed-loop kinematic chains in [13] and [41] include rubber and TPU links similar to the proposed mechanism outlined in Table 3, these studies did not investigate the energy absorption behavior, stiffness and vibration response analysis of the flexible element. On the other hand, these research works are covered in this study.

In comparison with [41], the new hybrid architecture presents higher rigidity and controllability, while in comparison with [33] it allows absorbing the energy, reducing the vibration and backlash. By considering the research presented in [13], [28], [29], [30], and [33], the proposed CDPM was identified through the FEA method, wherein the dynamic and stiffness response, as well as the kinematics were delineated, showcasing a diverse central limb structure.

Based on the experimental results, the integrated TPU elastic limb in both the hybrid limb (3-RRRR-1-F) and single elastic limb (1-F) mechanisms helped store maximum energy in the system, approximately 2.5 J and 1.9 J, respectively (see Fig. 10), when the CDPM was positioned vertically. However, despite the presence of minor friction at the revolute joints, force measurement along the tendon line driven by the motor in the 3-RRRR mechanism was unsuccessful. This is because the rigid limbs, lacking any flexible elements, could not resist the pulling motor. In other words, the 3-RRRR prototype does not exhibit elastic behavior, and this mechanism cannot accumulate sufficient energy when the platform is bent at a vertically oriented PM.

The central elastic TPU component functions like a spring, storing potential energy depending on its position. However, unlike an ideal spring, this material also dissipates energy when it is bent or extended.

When the vibration response analysis was performed at horizontal orientation, 1-F structure failed due to distortion of the TPU component (see Fig 11a) at an applied external stress, where this tends to lose the end-effector configuration located at the platform frame. Similarly, the 3-RRRR structure is more sensitive to the external applied torsional stress by having a higher vibration generated at the platform part if compared to the 3-RRRR-1F prototype. Finally, the stiffness of the 3-RRRR-1-F mechanism was analyzed, as it demonstrated superior performance and offered more

TABLE 3. List of sample state-of-the-art closed-loop kinematic chains with various designs and research works.

Robot structure (Research group)	Platform rotation (DOF)	Platform translation (x, y, z)	Number of actuators	Type of central limb	Presence of cables	Research works
3-PPR [11]	1	x, y	3	3 rigid limbs	Absent	Stiffness analysis of the planar PM at different base structures.
2SPR+RPS [12]	3	Absent	N/A	3 rigid limbs	Absent	Elastic deformation and stiffness analysis of the platform at various postures of the PM.
Liu et al [13]	3	Absent	4	1 rubber limb	4 cables	Testing the platform's load moment at various joint positions.
Parallel Continuum Robot (PCR) [14]	2	z	3	3 flexible glass legs	Absent	Workspace, stiffness and manipulability analysis; Development of the microminiature PM.
Bedoustani et al [15]	3	x, y, z	N/A	Absent	4 cables	Comparison of the dynamic behaviors of cables at various elasticity; Nonlinear dynamic analysis with Newton-euler formulation.
Modified Stewart-Gough type platform [16]	3	x, y, z	N/A	6 rigid legs	Absent	Testing the vibration and resonance response of the Stewart-Gough type PM with modified legs.
Cable-driven Continuum Robot (CDCR) [19]	2	Absent	N/A	1 flexible backbone	3 cables	Implementation of the static equilibrium, forward and inverse dynamic responses; Development of dynamic model based on Euler-Lagrange method.
Elsamanty et al [22]	3	Absent	3	3 rigid pair legs	Absent	Integration of the 3-RRS PM to the KUKA Kr6 R900; Workspace analysis and path planning tasks related to the hybrid manipulator.
Leijie et al [28]	2	Absent	3	1 flexible spring	3 cables	Vibration minimization with a nonlinear control method; Platform trajectory planning.
Yigit et al [29]	3	z	4	1 rigid sliding leg + 1 flexible spring	3 cables	Prediction of the spring compression and bending behaviors with FEA method; Stiffness analysis; Kinematic and dynamic modelling of the PM.
3-5R PM [30]	2	Absent	3	3 rigid legs + 1 flexible spring	3 cables	Prediction of the cable and spring stiffness; Development of the rigid-flexible mechanism associated with a spring.
Dong et al [32]	N/A	x, y, z	3	3 rigid parallelogram limbs	Absent	Development of position and force controlling strategies at the platform.
Kim et al [33]	3	Absent	3	3 rigid limbs	4 cables	Prediction of the high stiffness and low-inertia CDPM kinematics, manipulability and workspace.
Cybernetic shoulder [34]	3	Absent	3	3 rigid legs	Absent	Comparison of the damping and vibration absorption effects of cybernetic shoulder with variable link structures.
Otarbay et al [1]	2	Absent	3	3 rigid limbs	3 cables	Development of the Graphical User Interface (GUI) to control the PM in real and virtual environmental prototypes.
Yessirkepov et al [41]	2	Absent	3	1 elastic TPU limb	3 cables	Optimization of the TPU based central limb structure with FEA method; Development of the IK computation to predict the bending behavior of the elastic shoulder joint.
3-RRRR-1F shoulder joint	**2**	**Absent**	**3**	**1 elastic TPU limb + 3 rigid legs**	**3 cables**	**Stiffness and dynamic analysis; Testing the energy absorption behavior of elastic TPU limb and damping response of the system.**

advantages compared to both the 3-RRRR and 1-F structures based on previous experiments.

On the other hand, there are still gaps that must be solved with the designed hybrid (3-RRRR-1-F) shoulder joint associated with the experimental outcomes. All CDPMs with single cable motion were tested at vertically positioned configuration in Section IVA, but they were not validated at horizontally oriented configuration. Moreover, the three prototypes were tested by taking into account only 1 actuator motion. The question rises whether to test the system with all actuators activated simultaneously.

Meanwhile, the aluminum platform at 3-RRRR-1-F model weights 5-6 times heavier than 1-F model, which disturbs the formation of hysteresis in Fig. 9 and minimizes the energy absorption system in Fig. 10. In other words, as the platform with additional attachments at the end-effector frame becomes heavier, the central flexible element cannot resist against its load which can generate the risk of energy absorption failure in the system due to deformation issue of the TPU element.

According to the results obtained from the FEA, characterised in Section II, the resistance force of a thick and short TPU component against external loads is greater than that of a thin and long one, indicating that the thick and short TPU structure has a higher energy absorption capacity. However, the limited space between the rigid limbs and the overall height restricts design options. Reducing the height of the proposed CDPM would limit its workspace, and a thick TPU component could collide with the rigid limbs.

To address this, the rigid limbs would need to be spaced farther apart. This, in turn, could introduce another issue in the closed-loop kinematic system: a TPU element with high energy absorption capacity, when working again gravity, would require increased motor torque to pull the tendon line and bend the TPU attached to the platform. Therefore, it's preferable to construct a 3-RRRR-1-F manipulator with a thick elastic attachment and a platform as lightweight as possible, even though this configuration would consume more electrical power and energy from the actuator to store the energy generated by the TPU component in the system.

The amount of generated extra friction and backlash in the rigid limbs of the 3-RRRR-1-F structure should be minimized by smoothing the interface between the universal joint and rigid link attachments while ensuring they are not loosely connected.

The proposed 3-RRRR-1-F mechanism has 2 degrees of freedom (DOFs), enabling the platform to rotate in the roll and pitch directions and lacking rotation about the z-axis (Table 3). However, it is possible to design parallel mechanisms with more than 2 DOFs, similar to that described in [29]. To achieve this, an additional rigid link featuring two universal joints and one prismatic joint can be integrated within the elastic element. This configuration allows the central rigid element to rotate in the yaw direction and adjust the platform's height using a newly added central motor.

The central motor can be positioned at the base's bottom, oriented orthogonally to the other three actuators. Furthermore, the thickness of the TPU element must be increased and include a central hole to prevent interference with the additional central rigid limb housed within the elastic element. This design requires larger base and platform dimensions to accommodate the additional components.

An alternative approach to achieving a mechanism with more than 2 DOFs is to mount the central motor on top of the platform. This allows the base and platform dimensions to remain unchanged, although it increases the overall height of the parallel mechanism.

Another major drawback is the large size of the proposed mechanism, as all motors are mounted perpendicular to the tendon lines. (see Fig. 1). It would be more practical to design the structure with motors aligned parallel to the corresponding cable lines, despite the platform's 142 mm diameter. This approach would make it easier to mount the shoulder joint to the body of the humanoid robot. However, additional pulleys would be needed between each motor and tendon line in this parallel configuration, increasing maintenance work.

VI. CONCLUSION

In this research work, we presented a new design for a cable-driven parallel elastic shoulder joint, where a central limb made out of TPU material is combined with three lateral rigid limbs. Due to its compliance and flexibility, the TPU material is suitable for industrial applications, as it enhances manipulator precision, absorbs vibrations, and is less prone to breakage under certain stress levels compared to rigid materials. The kinematic structure in this study was approximated by combining two universal joints and one link. Three different prototypes of the shoulder joint were introduced and compared: 1) Single limb TPU (1-F) structure; 2) Three rigid limbs (3-RRRR) structure; 3) Hybrid limbs (3-RRRR-1-F) structure. The reason was to highlight which prototype has a kinematic and dynamic feasibility. After performing both kinematic and dynamic experiments, the hybrid limbs model outperformed in terms of withstanding against the external torsional forces and keeping the platform configuration in the home position without a significant backlash. Furthermore, the presence of the elastic central limb reduced the energy consumption while performing rotational movements. The actuation system of the shoulder joint was tested and its efficiency increased when it runs at a high velocity.

While analyzing the dynamic behavior of the servomotor, we observed that a significant amount of energy is used to pull the platform because the elastic central link resists the bending motion. However, part of this energy is stored and subsequently released when the shoulder joint returns to its home position. We also observed that the energy stored in the elastic central leg can be augmented by minimizing the platform weight and increasing the thickness of the elastic element. The thickness of the TPU element must be optimized to avoid collisions with the rigid limbs, and the motors in the system must have enough power to pull the tendon line against the resistance from the TPU component.

Since each cable-driven parallel manipulator (CDPM) prototype's platform diameter exceeds 1 decimeter and is equipped with powerful servomotors (see Fig. 1), they may be more fitting for the shoulder or hip joint rather than the wrist section of the humanoid robot. Yet, for its utilization as a wrist joint, dimension reduction becomes imperative.

Future work will examine the damping capabilities and deformation of the TPU material under applied external forces, considering variations in its thickness and height. Additionally, this type of component will be installed at the ankle of a bipedal robot for energy absorption and damping purposes. We aim to augment the proposed shoulder joint by reducing its dimensions and adding a fourth servomotor, thereby creating a 3-DOF mechanism suitable for use as the shoulder joint in a humanoid robot.

DECLARATION OF GENERATIVE AI USAGE

During the preparation of this manuscript the authors used ChatGPT-3.5 exclusively to improve the readability and the grammar of some of the sentences. After using this tool, the authors reviewed and edited the content as needed and take full responsibility for the content of the publication.

REFERENCES

[1] Z. Otarbay, S. Yessirkepov, T. Ishuov, and M. Folgheraiter, "Development of a shoulder joint for humanoid robotics application," in *Proc. 20th Int. Conf. Adv. Robot. (ICAR)*, Dec. 2021, pp. 771–776.

[2] J. P. Merlet, *Parallel Robots*, 2nd ed., Cham, Switzerland: Springer, 2010.

[3] R. Clavel, "DELTA, a fast robot with parallel geometry," in *Proc. 18th Int. Symp. Ind. Robots*, C. W. Burckhardt, Ed., Springer-Verlag, 1988, pp. 91–100.

[4] R. B. Hertz and P. C. Hughes, "Kinematic analysis of a general double-tripod parallel manipulator," *Mechanism Mach. Theory*, vol. 33, no. 6, pp. 683–696, Aug. 1998.

[5] S. Sakurai and S. Katsura, "6-DOF hybrid cable-driven parallel robot with an articulated manipulator," in *Proc. IEEE 33rd Int. Symp. Ind. Electron. (ISIE)*, Jun. 2024, pp. 1–6.

[6] A. E. Huisjes and V. van der Wijk, "Compliant manipulator design method (COMAD) for the type synthesis of all serial and parallel multi-DoF compliant mechanisms, with example of a Schönflies motion generator," *Mechanism Mach. Theory*, vol. 186, Aug. 2023, Art. no. 105342.

[7] J. Wang and C. M. Gosselin, "Kinematic analysis and design of kinematically redundant parallel mechanisms," *J. Mech. Des.*, vol. 126, no. 1, pp. 109–118, Jan. 2004.

[8] H. Jamshidifar, B. Fidan, G. Gungor, and A. Khajepour, "Adaptive vibration control of a flexible cable driven parallel robot," *IFAC-PapersOnLine*, vol. 48, no. 3, pp. 1302–1307, 2015.

[9] C. Li, X. Gu, X. Xiao, C. M. Lim, and H. Ren, "A robotic system with multichannel flexible parallel manipulators for single port access surgery," *IEEE Trans. Ind. Informat.*, vol. 15, no. 3, pp. 1678–1687, Mar. 2019.

[10] L. Luo, S. Wang, J. Mo, and J. Cai, "On the modeling and composite control of flexible parallel mechanism," *Int. J. Adv. Manuf. Technol.*, vol. 29, nos. 7–8, pp. 786–793, Jul. 2006.

[11] X. Wu, Y. Wang, Z. Xiang, R. Yan, R. Shu, and R. Tan, "Stiffness analysis of a 3-DOF parallel manipulator with variable geometry platforms," in *Proc. IEEE Int. Conf. Mechatronics Autom. (ICMA)*, Oct. 2020, pp. 723–728.

[12] N. Zhang, "Stiffness analysis of a 3-DOF 2SPR+RPS parallel manipulator," in *Proc. 11th Int. Conf. Intell. Hum.-Mach. Syst. Cybern. (IHMSC)*, vol. 2, Aug. 2019, pp. 76–79.

[13] F. Liu, B. Li, H. Huang, and Y. Ning, "Design and analysis of a lightweight flexible cable-driven manipulator," in *Proc. IEEE 9th Annu. Int. Conf. CYBER Technol. Autom., Control, Intell. Syst. (CYBER)*, Jul. 2019, pp. 708–712.

[14] C. Nwafor, G. J. Laurent, and K. Rabenorosoa, "Miniature parallel continuum robot made of glass: Analysis, design, and proof-of-concept," *IEEE/ASME Trans. Mechatronics*, vol. 28, no. 4, pp. 2038–2046, Apr. 2023.

[15] Y. B. Bedoustani, H. D. Taghirad, and M. M. Aref, "Dynamics analysis of a redundant parallel manipulator driven by elastic cables," in *Proc. 10th Int. Conf. Control, Autom., Robot. Vis.*, Dec. 2008, pp. 536–542.

[16] E. Natarajan, A. R. Venkataramanan, R. Sasikumar, S. Parasuraman, and G. Kosalishkwaran, "Dynamic analysis of compliant LEG of a Stewart–Gough type parallel mechanism," in *Proc. IEEE Student Conf. Res. Develop. (SCOReD)*, Oct. 2019, pp. 123–128.

[17] J. Hu, "Vibration suppression of a high-speed flexible parallel manipulator based on its inverse dynamics," in *Proc. 2nd Int. Conf. Intell. Syst. Design Eng. Appl.*, Jan. 2012, pp. 744–747.

[18] P. Rao and A. D. Deshpande, "Analyzing and improving Cartesian stiffness control stability of series elastic tendon-driven robotic hands," in *Proc. IEEE Int. Conf. Robot. Autom. (ICRA)*, May 2018, pp. 5415–5420.

[19] A. Amouri, C. Mahfoudi, and A. Zaatri, "Dynamic modeling of a spatial cable-driven continuum robot using Euler–Lagrange method," *Int. J. Eng. Technol. Innov.*, vol. 10, no. 1, pp. 60–74, Jan. 2020.

[20] S. A. Khalilpour, H. D. Taghirad, and H. Habibi, "Wave-based control of suspended cable driven parallel manipulators," in *Proc. 5th Int. Conf. Control, Instrum., Autom. (ICCIA)*, Nov. 2017, pp. 173–178.

[21] A. Arena, E. Ottaviano, and V. Gattulli, "Dynamics of cable-driven parallel manipulators with variable length vibrating cables," *Int. J. Non-Linear Mech.*, vol. 151, May 2023, Art. no. 104382.

[22] M. Elsamanty, E. M. Faidallah, Y. H. Hossameldin, S. A. Rabbo, S. A. Maged, H. Yang, and K. Guo, "Workspace analysis and path planning of a novel robot configuration with a 9-DOF serial–parallel hybrid manipulator (SPHM)," *Appl. Sci.*, vol. 13, no. 4, p. 2088, Feb. 2023.

[23] X. Zhang, C. Cao, K. Luo, Z. Wu, K. Qin, M. An, W. Ding, and W. Xiang, "Design and operation of a Peucedani Radix weeding device based on YOLOV5 and a parallel manipulator," *Frontiers Plant Sci.*, vol. 14, May 2023, Art. no. 1171737.

[24] H. Nigatu and D. Kim, "Workspace optimization of 1T2R parallel manipulators with a dimensionally homogeneous constraint-embedded Jacobian," *Mechanism Mach. Theory*, vol. 188, Oct. 2023, Art. no. 105391.

[25] L. Kong, G. Chen, H. Wang, G. Huang, and D. Zhang, "Kinematic calibration of a 3-PRRU parallel manipulator based on the complete, minimal and continuous error model," *Robot. Computer-Integrated Manuf.*, vol. 71, Oct. 2021, Art. no. 102158.

[26] X. Yuan, Q. Meng, F. Xie, X.-J. Liu, and J. Wang, "Error modeling and accuracy evaluation of parallel manipulators with mixed DoFs based on motion/force transmissibility and constrainability," *Mechanism Mach. Theory*, vol. 186, Aug. 2023, Art. no. 105346.

[27] E. Ottaviano, A. Arena, and V. Gattulli, "Geometrically exact three-dimensional modeling of cable-driven parallel manipulators for end-effector positioning," *Mechanism Mach. Theory*, vol. 155, Jan. 2021, Art. no. 104102.

[28] L. Jiang, B. Gao, and Z. Zhu, "Design and nonlinear control of a 2-DOF flexible parallel humanoid arm joint robot," *Shock Vibrat.*, vol. 2017, pp. 1–14, Sep. 2017.

[29] C. B. Yigit and P. Boyraz, "Design and modelling of a cable-driven parallel-series hybrid variable stiffness joint mechanism for robotics," *Mech. Sci.*, vol. 8, no. 1, pp. 65–77, Mar. 2017.

[30] F. Liu, H. Huang, B. Li, Y. Hu, and H. Jin, "Design and analysis of a cable-driven rigid–flexible coupling parallel mechanism with variable stiffness," *Mechanism Mach. Theory*, vol. 153, Nov. 2020, Art. no. 104030.

[31] G. Hassan, M. Gouttefarde, A. Chemori, P.-E. Hervé, M. E. Rafei, C. Francis, and D. Sallé, "Time-optimal pick-and-throw S-curve trajectories for fast parallel robots," *IEEE/ASME Trans. Mechatronics*, vol. 27, no. 6, pp. 4707–4717, Dec. 2022.

[32] H. Dong, Y. Feng, C. Qiu, and I.-M. Chen, "Construction of interaction parallel manipulator: Towards rehabilitation massage," *IEEE/ASME Trans. Mechatronics*, vol. 28, no. 1, pp. 372–384, Feb. 2023.

[33] Y.-J. Kim, J.-I. Kim, and W. Jang, "Quaternion joint: Dexterous 3-DOF joint representing quaternion motion for high-speed safe interaction," in *Proc. IEEE/RSJ Int. Conf. Intell. Robots Syst. (IROS)*, Oct. 2018, pp. 935–942.

[34] M. Okada, Y. Nakamura, and S. Hoshino, "Development of the cybernetic shoulder—A three DOF mechanism that imitates biological shoulder-motion," in *Proc. IEEE/RSJ Int. Conf. Intell. Robots Syst. Human Environ. Friendly Robots High Intell. Emotional Quotients*, vol. 1, Oct. 1999, pp. 543–548.

[35] B. Zhao, X. Zhang, Z. Zhan, Q. Wu, and H. Zhang, "A novel semi-supervised graph-guided approach for intelligent health state diagnosis of a 3-PRR planar parallel manipulator," *IEEE/ASME Trans. Mechatronics*, vol. 27, no. 6, pp. 4786–4797, Dec. 2022.

[36] M. Folgheraiter, S. Yessirkepov, and A. Yessaly, "An actuated spherical joint for humanoid robotics applications," in *Proc. IEEE Int. Conf. Cybern. Intell. Syst. (CIS) IEEE Conf. Robot., Autom. Mechatronics (RAM)*, Nov. 2019, pp. 571–576.

[37] M. Gürgöze, "On the eigenfrequencies of a cantilever beam with attached tip mass and a spring-mass system," *J. Sound Vib.*, vol. 190, no. 2, pp. 149–162, Feb. 1996.

[38] N. P. Sorimpuk, W. H. Choong, and B.-L. Chua, "Thermoforming characteristics of PLA/TPU multi-material specimens fabricated with fused deposition modelling under different temperatures," *Polymers*, vol. 14, no. 20, p. 4304, Oct. 2022.

[39] C. Emminger, U. D. Çakmak, R. Preuer, I. Graz, and Z. Major, "Hyperelastic material parameter determination and numerical study of TPU and PDMS dampers," *Materials*, vol. 14, no. 24, p. 7639, Dec. 2021.

[40] Y. Jiang, K. Shi, L. Zhou, M. He, C. Zhu, J. Wang, J. Li, Y. Li, L. Liu, D. Sun, G. Feng, Y. Yi, and L. Zhang, "3D-printed auxetic-structured intervertebral disc implant for potential treatment of lumbar herniated disc," *Bioactive Mater.*, vol. 20, pp. 528–538, Feb. 2023.

[41] S. Yessirkepov, T. Umurzakov, R. Shaimerdenov, and M. Folgheraiter, "An elastic shoulder joint for humanoid robotics application," in *Proc. 9th Int. Conf. Autom., Robot. Appl. (ICARA)*, Feb. 2023, pp. 117–122.

[42] M. Folgheraiter, T. Umurzakov, and S. Yessirkepov, "A servomotor with adjustable stiffness for humanoid robotics application," in *Proc. ACTUATOR, Int. Conf. Exhib. New Actuator Syst. Appl.*, Jun. 2022, pp. 1–4.

[43] J. Craig, *Introduction to Robotics: Mechanics and Control*. Reading, MA, USA: Addison-Wesley, 1986.

[44] M. Toz, H. Han, and J. Angeles, "Workspace, singularity, and dexterity analyses of a six-degrees-of-freedom SDelta robot with an orthogonal base platform," *J. Mech. Robot.*, vol. 16, no. 7, Jul. 2024, Art. no. 071010.
[45] L. Wang and Y. Li, "Singularity of a novel five-DOF parallel manipulator," in *Proc. 2nd Int. Conf. Ind. Mechatronics Autom.*, May 2010, pp. 240–243.
[46] L.-W. Tsai, *Robot Analysis and Design: The Mechanics of Serial and Parallel Manipulators*, 1st ed., Hoboken, NJ, USA: Wiley, 1999.
[47] H. Zhang, J. Tang, C. Yan, G. Cui, M. Zhang, and Y. Yao, "Stiffness analysis of a 3-DOF parallel mechanism for engineering special machining," *Mech. Sci.*, vol. 13, no. 2, pp. 635–645, Jul. 2022.

SHARAFATDIN YESSIRKEPOV received the B.Sc. degree from Kazakh National Research Technical University, in 2010, and the M.Eng. degree from the University of Alberta, in 2014. He is currently pursuing the Ph.D. degree in robotics with Nazarbayev University. His research interests include teleoperation systems, humanoid robotics, and parallel manipulators.

TIMUR UMURZAKOV received the B.Sc. degree from Kazakh National Research Technical University, in 1995, and the M.A. degree in public administration from the Kazakh Institute of Management, Economics and Strategic Research (KIMEP), in 1999. He is currently pursuing the Ph.D. degree in robotics with Nazarbayev University. His research interests include robot dynamics and control, humanoid robotics, and neural networks.

MICHELE FOLGHERAITER (Member, IEEE) received the M.S. degree in computer engineering with major in automation systems and the Ph.D. degree in information technology from the Politecnico di Milano, in 2000 and 2004, respectively. From 2002 to 2007, he held the positions of an Adjunct Researcher and a Teaching Assistant in robotics with the Politecnico di Milano. From 2008 to 2013, he was with the German Research Center for Artificial Intelligence (DFKI) as a Senior Researcher. Since 2013, he has been with the Department of Robotics, Nazarbayev University, as an Associate Professor. His research interests include humanoid robotics, haptic interfaces, and bio-inspired control systems.